Charged Particle Fluxes Associated With CALIPSO Low Laser Energy Shots

J. V. Rodriguez, R. C. Verhappen, C. Weimer, C. R. Trepte, and T. E. Cayton

***Abstract*— The cloud-aerosol lidar and infrared pathfinder satellite observation (CALIPSO) mission was launched on 28 April 2006 into a 705-km Sun-synchronous orbit. At launch, the lidar laser canisters were filled with dry air at 130 kPa. The redundant canister pressure has dropped during the mission, reaching 7.6 kPa by late December 2021. Starting on June 23, 2016, individual laser shots started to exhibit anomalously low energies in regions of enhanced energetic charged particle fluxes. Small at first (<1 mJ), drops in laser energy up to 61 mJ have been observed. This study determines the energetic charged particle populations associated spatially with low laser energy shots and the degree to which time variations in the low laser energy shots can be explained by time variations in the energetic charged particle fluxes. Particle observations from the NOAA-19 medium energy proton and electron detector (MEPED) are traced down magnetic field lines to estimate the fluxes at CALIPSO altitudes that are associated with individual low-energy shots. Predictions of the stability of particle bounce and drift motions in the geomagnetic field are used to sort low-energy shots and fluxes into different radiation belt regions. While most of the low-energy shots occur in the inner belt, there are clear spatial associations with outer belt electrons and with galactic cosmic rays (GCRs). As canister pressure has decreased, GCRs and electrons have become more effective in causing larger laser energy drops.**

***Index Terms*— Cloud-aerosol lidar and infrared pathfinder satellite observation (CALIPSO), galactic cosmic rays (GCRs), ionizing radiation, lidar, low-Earth orbit (LEO), medium energy proton and electron detector (MEPED), radiation belts.**

I. Introduction

SATELLITES in polar orbits at low altitudes pass through regions of energetic charged particle radiation that present a hazard to flight hardware and interfere with the proper operation of scientific instruments. These populations respond in a wide variety of ways to geomagnetic and solar activity and exhibit different altitude variations. Effects of these populations include upsets in electronics and false counts in detectors [1], [2], [3], [4], [5], [6]. Although such effects are well known through repeated experience and can be mitigated to a certain degree through design, testing and operations, new susceptibilities may be discovered when innovative hardware is introduced to the space environment. This article reports on one such new susceptibility.

The cloud-aerosol lidar and infrared pathfinder satellite observation (CALIPSO) mission was launched on 28 April 2006 into a 705-km Sun-synchronous orbit with a 1330 local time ascending node (LTAN). Originally planned for a three-year mission, CALIPSO continues to make high-quality scientific measurements after 16 years on orbit. The primary payload is the cloud-aerosol lidar with orthogonal polarization (CALIOP), which includes a primary and a redundant laser [7]. The redundant laser has been in use since February 2009. At launch, the CALIOP laser canisters (primary and redundant) were filled with dry air at 130 kPa (19 psia; 1 standard atmosphere is 101.325 kPa). The canister pressure has dropped approximately exponentially during the mission, reaching 7.6 kPa (1.1 psia) by late December 2021. Starting on June 23, 2016, after the pressure reached a third of an atmosphere, individual laser shots started to exhibit low energies in regions of enhanced energetic charged particle fluxes, predominantly within the South Atlantic Anomaly (SAA). Small at first (<1 mJ), the maximum drop magnitude has grown to be as great as 61 mJ. The cause in the laser of the low-energy shots is understood and has been seen in both the primary and redundant laser after each had been on for an extended period. It is not understood, however, how the interaction with the radiation environment occurs. CALIPSO utilizes a laser energy telemetry data channel measured at the output of the laser in addition to the primary science channels measured after scattering from the atmosphere. These data channels are independent. Comparisons between the data channels isolates the source of the energy drops to the actual optical output of the laser. Although single event effects (SEEs) in the laser drive electronics cannot be completely ruled out, prelaunch analyses and on-board monitoring circuits indicate the most likely cause is isolated to the actual laser and a likely source identified. NASA Langley Research Center has issued an advisory for data users on how to identify and treat low laser energy shots [8].

This study addresses two key questions as follows.

1) What are the energetic charged particle populations associated spatially with CALIOP low laser energy shots?
2) To what degree can time variations in the the CALIOP low laser energy shots be explained by time variations in the energetic charged particle fluxes?

Manuscript received 11 June 2022; revised 12 August 2022; accepted 19 August 2022. Date of publication 23 September 2022; date of current version 18 October 2022. This work was supported in part by the National Aeronautics and Space Administration (NASA) under Contract 80LARC21F0023 Mod 003 and in part by the National Oceanic and Atmospheric Administration (NOAA) Cooperative Agreement with the Cooperative Institute for Research in Environmental Sciences (CIRES) under Grant NA17OAR4320101.

J. V. Rodriguez was with Ball Aerospace, Boulder, CO 80301 USA. He is now with CIRES, University of Colorado, Boulder, CO 80309 USA (e-mail: juan.v.rodriguez@colorado.edu).

R. C. Verhappen is with Science Systems and Applications, Inc., Hampton, VA 23681 USA (e-mail: ron.verhappen@nasa.gov).

C. Weimer is with Ball Aerospace, Boulder, CO 80301 USA (e-mail: carl.weimer@ballaerospace.com).

C. R. Trepte is with the NASA Langley Research Center, Hampton, VA 23681 USA (e-mail: charles.r.trepte@nasa.gov).

T. E. Cayton, retired, was with the Los Alamos National Laboratory, Rio Rancho, NM 87144 USA (e-mail: th23cayton@gmail.com).

Color versions of one or more figures in this article are available at https://doi.org/10.1109/TNS.2022.3204715.

Digital Object Identifier 10.1109/TNS.2022.3204715

The predominance of effects within the SAA suggests that the effects are related to the penetration of energetic particles through the walls of the canister. In order to identify the associated charged particle populations, we have used observations by the NOAA-19 (N19) Space Environment Monitor (SEM)-2 of proton and electron fluxes that are sufficiently energetic to penetrate the canister walls. After describing the datasets and analysis methods, we show the results of spatial and time-series analyses, draw some conclusions based on the observations, and identify possible investigation paths.

II. Data

A. CALIOP Laser Energies and Pressures

In this article, energy drops from the 1064-nm laser are analyzed. The energy-drop data downloaded from the payload consist of 15-shot averages sent down every 5 s. The duration of each shot is 20 ns, and the repetition rate is 20.16 Hz. The energy drops analyzed here are corrected from the on-board estimate using a pre-flight calibration over a large range of energies. The laser energies are included in the CALIPSO data products [9]. The "best" pressure estimate for the redundant laser canister changed from the average of two pressure sensors to just the data from sensor 1 on December 1, 2017. The pressure has been fit to an exponential whose argument is a quadratic polynomial of time.

B. NOAA-19 Particle Data

The charged particle dataset is from the N19 medium energy proton and electron detector (MEPED) omnidirectional (omni) charged particle detectors, which are part of the SEM-2 suite [10], [11]. N19 was chosen because it has a similar LTAN to CALIPSO and because its data span the period of low laser energy shots. The omni fields-of-view are centered on the zenith direction. Although intended to monitor MeV proton fluxes, the omnis are also sensitive to MeV electrons [12], [13], [14], [15]. The lowest proton and electron energies to which the omnis are sensitive are summarized in Table I.

Electrons and protons of sufficient energy penetrate the canister structure and deposit energy in the gas by ionizing it. Bremsstrahlung photons emitted by electrons slowing down or stopping in the canister structure or gas also ionize the gas. Using 6.35 mm (250 mils) of aluminum as representative of the shielding, >40 MeV protons and >3 MeV electrons penetrate to the gas. These lower energies correspond most closely to the lower energies of the P7 detector for proton fluxes and the P6 detector for electron fluxes. In N19 observations during the period of interest, electron fluxes are very low to negligible in the SEM-2 omni directors other than P6, while inner belt proton, solar proton, and galactic cosmic ray (GCR) proton fluxes are detected by all four omni detectors.

An example of N19 P6 omnidirectional detector count rates averaged over one month is shown in Fig. 1, along with contours of L_m, the McIlwain L-parameter [16] (see Section III-B for the calculation of L_m). The inner belt count rates are dominated by >16 MeV protons while the outer belt count rates are dominated by >3 MeV electrons. Striations in the northern and southern hemisphere outer belts indicate transiently large measurements from individual orbits. The outer belt is not always observed so clearly in this channel. Its observation indicates recent radiation belt growth and transport to lower $L-$shells. The outer belt footprint that extends below $L = 3$ originated in a radiation belt enhancement that started on September 8, diffused to lower L-shells and persisted through October and into November, as observed by Van Allen Probes [17]. This is one of several outer belt enhancements that have caused CALIOP low laser energy shots.

TABLE I
MEPED Omnidirectional Detector Minimum Energies [10], [13]

Detector	Proton (MeV)	Electron (MeV)
P6	16	3
P7	35	6
P8	70	above 10
P9	140	above 10

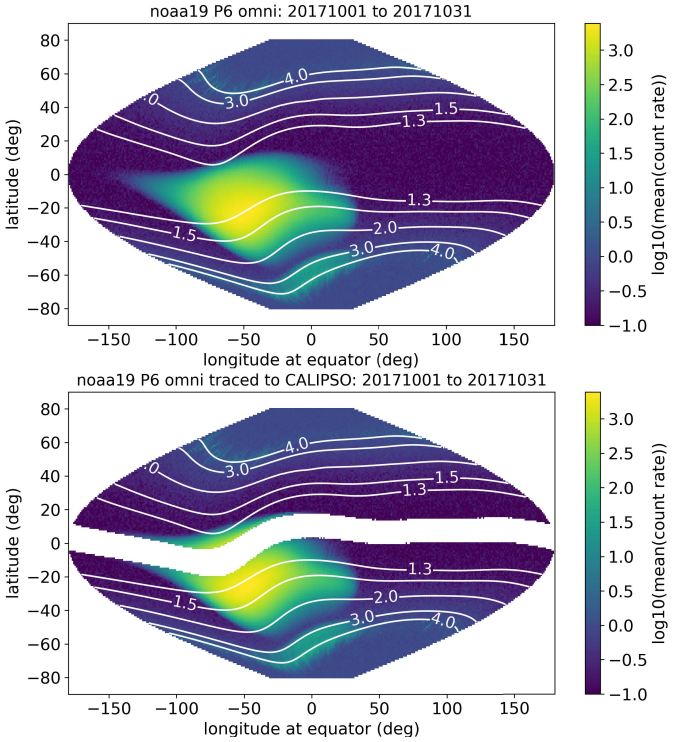

Fig. 1. Monthly averages from October 2017 of NOAA-19 MEPED omnidirectional P6 count rates as observed (top) and as traced to 700 km (bottom). The rates are averaged in $1^\circ \times 1^\circ$ bins at the equator, with the longitudinal bin size increasing with latitude to maintain a constant solid angle.

III. Analysis Methods

A. Mapping NOAA-19 Data to CALIPSO Altitude

The N19 locations were mapped to CALIPSO altitude by tracing along magnetic field lines in the same hemisphere using the "find_footprint" function from the irbempy module of SpacePy [18], [19]. The International Geomagnetic Reference Field (IGRF) multipolar internal field model was used without an external field model. These mapping results were used to match each laser energy drop to a four-week temporal

and 1° × 1° spatial average of N19 MEPED omni count rates. This averaging period was tailored to the sparseness of GCR observations and may smear out the variability of outer belt fluxes, but this is not important for the spatial associations. (A different period, three days, was used to calculate the time series discussed in Section IV-C.) This geomagnetic mapping leaves an unpopulated band at 700 km at the lowest geomagnetic latitudes, where the field lines do not link 850 km altitudes. An example of a P6 count rate map traced to 700 km is shown in Fig. 1. This modeling does not include the decrease in omnidirectional fluxes with increasing field strength; in fact, >40 MeV proton fluxes observed at 700 km are approximately a factor of 3 lower than at 850 km [20].

B. Spatially Filtering CALIPSO and NOAA-19 Data by Radiation Trapping Region

The parameters L_m and L^* were calculated to determine whether particles are stably trapped, quasi-trapped, or not trapped by the geomagnetic field at the CALIPSO altitude. The boundaries of these trapping regions were used to spatially filter the CALIPSO data and the traced N19 data using methods developed for geographic information systems (GISs). In a dipolar magnetic field, L_m is the radial distance in Earth radii at which a field line crosses the equator. A generalized form of L_m, L^* is the equatorial radial distance of the drift shell on which fluxes would be located if all nondipolar components of the field were slowly turned off [21]. The irbempy function "get_Lstar" was used to calculate L_m and L^*. If "get_lstar" returns $L_m < 0$, locally observed fluxes precipitate into the opposite hemisphere after mirroring locally. If "get_Lstar" returns $L^* < 0$, locally observed fluxes precipitate in the SAA after drifting around the Earth. If both parameters are returned as negative, the observed fluxes are untrapped. If $L_m > 0$ and $L^* < 0$, the fluxes are quasi-trapped. If both L_m and L^* are positive, the fluxes are stably trapped, i.e., they remain trapped after a single bounce and after a complete drift around the Earth. A local 90° (mirroring) pitch angle was assumed for this analysis.

The trapping regions were calculated at 700 and 850 km using the internal IGRF model for October 15, 2017, by calculating L_m and L^* on a 1° grid at the equator, with the longitudinal width increasing as the inverse of the cosine of latitude in order to have cells of approximately constant solid angle (in order to avoid exaggerating the size of the regions at higher latitudes). The finest angular resolution along the field line and in azimuth was used to avoid artificial ripples in the region boundaries. Each cell was assigned a code according to whether the particles were untrapped, quasi-trapped, or stably trapped. The stably trapped regions were divided into $L < 2$ for the inner belt, $2 \leq L < 6.5$ for the slot region and outer belt, and $L \geq 6.5$ for regions not well modeled by an internal-only field model and therefore excluded from this analysis (the yellow regions at higher latitudes in the figure). By comparing Fig. 2 with Fig. 1, it becomes clear that the monthly averages of N19 observations are dominated by stably-trapped fluxes. The trapping regions are smaller at 700 km than at 850 km. The 700 km trapping regions were used to determine which observations lie within the stably trapped regions. The 850 km trapping regions were used to determine data within the untrapped or quasi-trapped regions. Data from in between were excluded from the analysis because trapped fluxes at the edges of the 850-km trapping regions mirror above 700 km, and transient precipitating fluxes do not contribute substantially to the four-week averages.

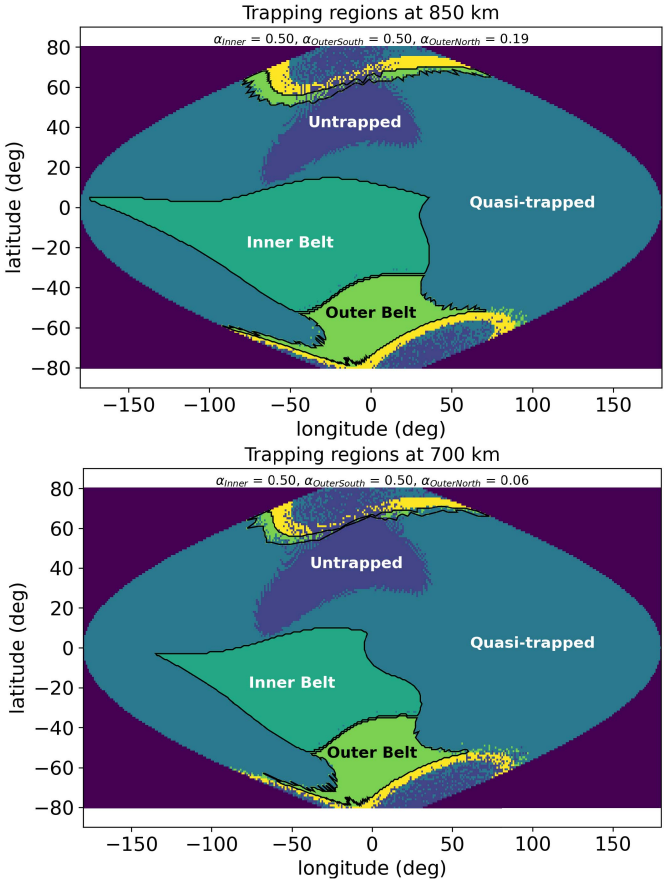

Fig. 2. Trapping regions at 850 km (top) and 700 km (bottom) calculated using irbempy. The dark outlines are the bounding polygons (concave hulls) used to spatially filter the data. See text for details of the calculations.

To spatially filter the time series of energy drops and fluxes by trapping region, we used two Python libraries. We used "alphashape" to create concave hulls (bounding polygons) around the trapping regions, and we imported these concave hulls into "shapely" to filter the data by latitude and longitude. (The α parameters that characterize the concave hulls are reported in the title of each panel.) The concave hulls were converted to the polygon class, and each data point was converted to the point class. Then it was a matter of determining which polygon contains a given point. (Concave rather than convex hulls were used because concave hulls better follow the (sometimes irregular) edges of the trapping regions determined from the irbempy results.)

IV. Results

A. Maps of Particles Associated With Low Laser Shot Energies

Maps of P6 count rates associated with energy drops from October 2017 (see Fig. 3) and November 2021 (see Fig. 4)

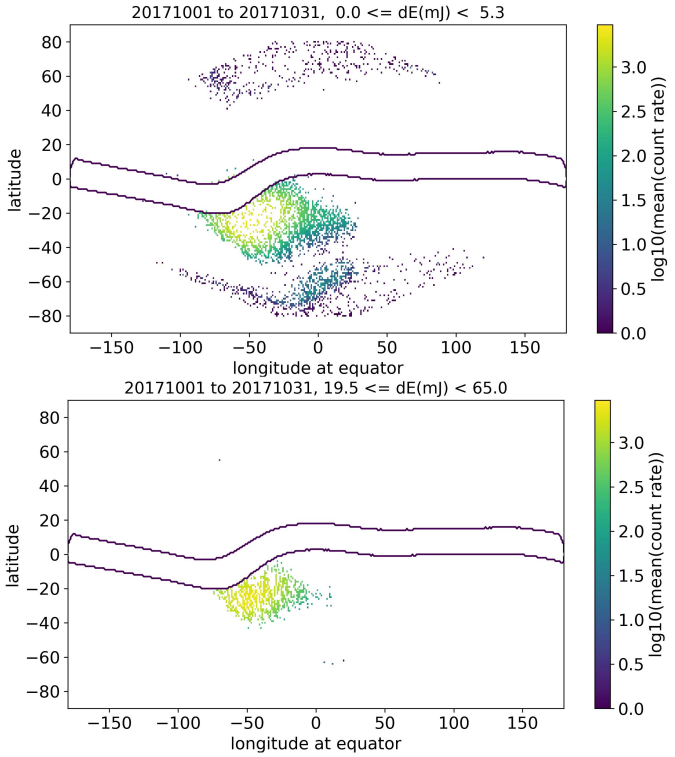

Fig. 3. NOAA-19 MEPED P6 omni count rates associated with energy drops in two bins [<5.3 mJ (top) and 19.5–65 mJ (bottom)] during October 2017. The color scale represents the base-10 logarithm of P6 count rates, averaged in time and space as described in the text.

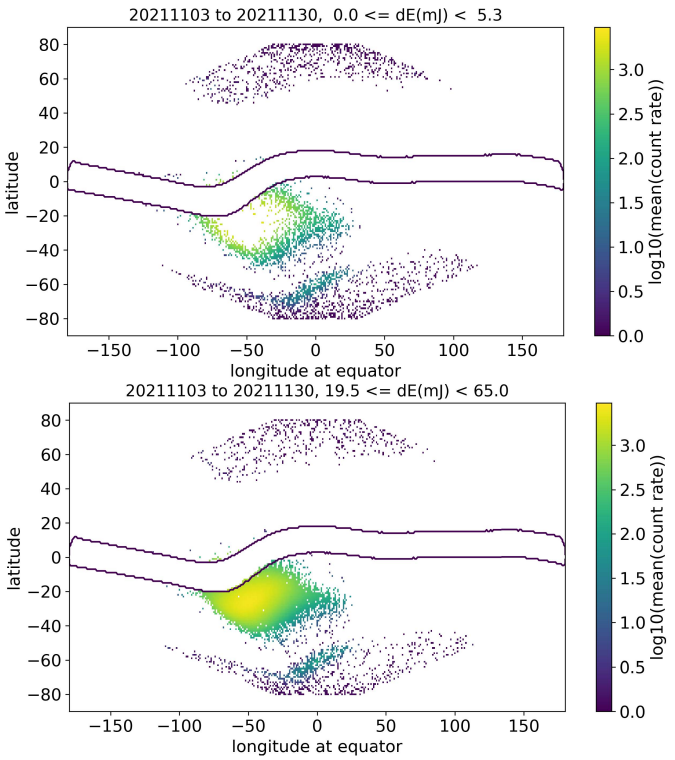

Fig. 4. NOAA-19 MEPED P6 omni count rates associated with energy drops in two bins [<5.3 mJ (top) and 19.5–65 mJ (bottom)] during November 2021.

illustrate the spatial distribution of energy drops and their variation with size and time. The smallest (<5.3 mJ) and largest (>19.5 mJ) energy drop bins are shown. During October 2017, when the canister pressure was 25.5 kPa (3.7 psia), two spatial patterns are evident (see Fig. 3). First, particles with low linear energy transfer (LET) (electrons in the outer belt, GCRs at high latitudes) are associated with energy drops <5.3 mJ. This association is largely absent at larger energy drops. Second, the spatial distribution of drops in the SAA is hollow in smaller energy drop bins. The distribution shrinks and fills in as the size of energy drops increases.

By November 2021, the canister pressure had dropped to 9.0 kPa (1.3 psia). This month is shown because, as in October 2017, the outer belt >3 MeV electron population is enhanced. The number of energy drops has increased greatly, and, in striking contrast to October 2017, low-LET particles are associated with all sizes of energy drops (see Fig. 4). As before, the spatial distribution of energy drops in the SAA is hollow at lower sizes and is filled in at greater sizes. However, in contrast to 2017, the extent of drops in the SAA is approximately constant with the magnitude of energy drop.

B. Change With Time of Energy Drop Histograms

The time dependence indicated by the maps shown in Section IV-A suggests that the distribution of energy drops by drop magnitude has flattened with time. This is illustrated in Fig. 5 in one-year intervals. In October 2016–2018, the histogram of energy drops was steep. By October 2019, the

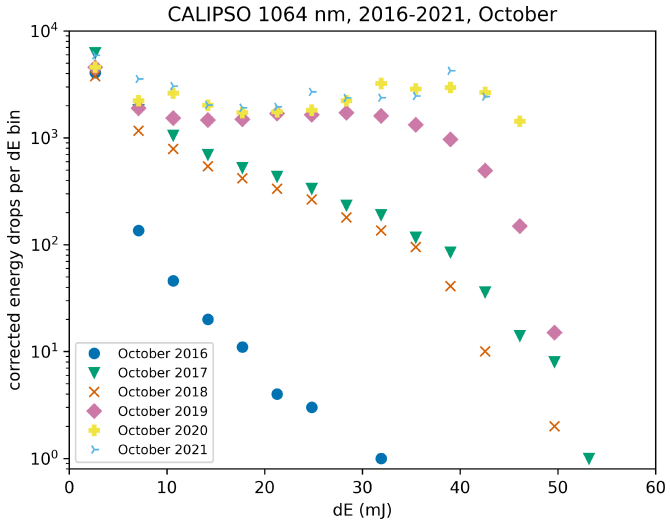

Fig. 5. Histograms of energy drop (dE) magnitudes over all locations for October in 2016–2021.

distribution was flat out to 35 mJ. The roll off above 35 mJ, dramatic in October 2019, has greatly decreased since then. In October 2021, the difference in the distribution between the smallest and largest energy drops was only a factor of 3.

In Fig. 6, the distributions for October 2017 and November 2021 are sorted by the mapped N19 omni P6 count rates and normalized to the total number of drops in each energy drop bin. (Although the lower proton energy of P7 is more representative than P6 of the canister shielding, the plots are

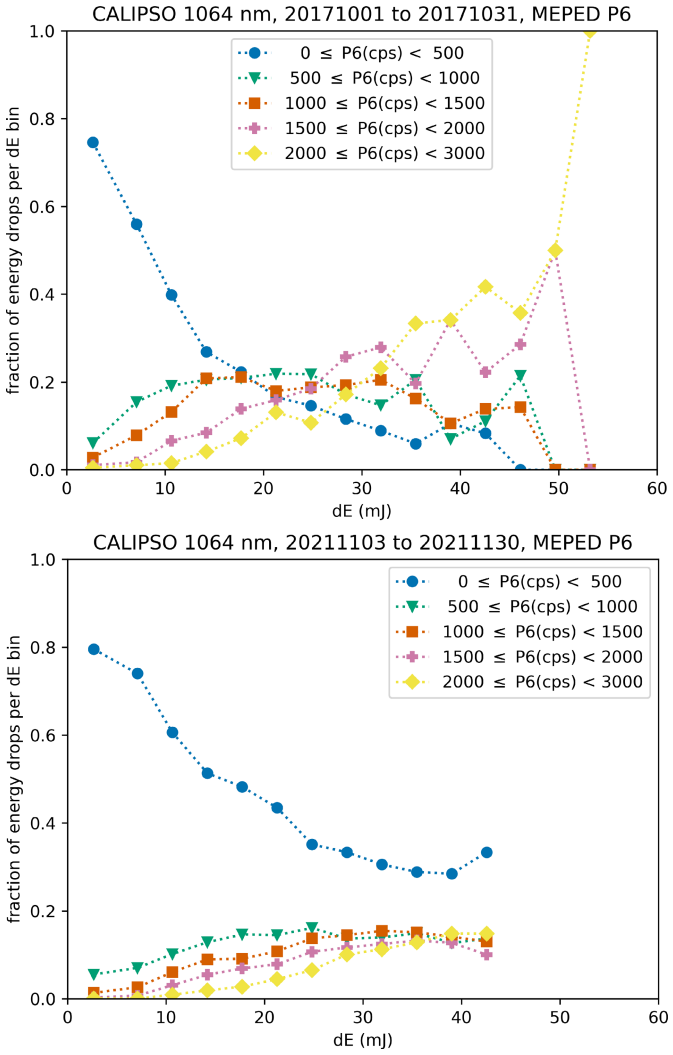

Fig. 6. Fractions of energy drops (dE) as a function of energy drop magnitudes over all locations for October 2017 (top) and November 2021 (bottom). Each curve corresponds to a range of NOAA-19 MEPED omni P6 count rates, traced to CALIPSO altitude and averaged as described in the text.

similar when sorted by P7 count rates.) Several behaviors are evident as follows.

1) The lowest count rate range (<500 cps) has always dominated the smallest energy-drop bin. In November 2021, it was the most effective count rate range in all energy-drop bins.
2) The highest count rate range (2000–3000 cps) dominated the largest energy-drop bins early on. At present, it is less effective than the lowest count rate range and similarly effective to the other ranges in causing the largest energy drops.
3) The energy drop bin in which the selected count rate ranges are most similarly effective in causing energy drops has increased with time, from 21 mJ in October 2017 to 39 mJ in November 2021 (apart from the lowest count rate range).

C. Time Series of Energy Drops and Particle Fluxes

Time series of CALIOP low laser energy shots and N19 particle fluxes were compared to determine whether fluctuations in the rate of low-energy shots were associated with changes in the fluxes of energetic charged particles (see Fig. 7). As discussed earlier, the trapping region boundaries were used to spatially filter and average the two time series. The boundaries at 700 km were used to isolate the time series in the inner belt ($L \leq 2$) and in the outer belt ($2 < L \leq 6.5$). The northern and southern hemisphere outer belt regions were evaluated separately. The boundaries at 850 km were used to isolate the time series in untrapped and quasi-trapped regions while reducing spurious contributions from the fluxes at the edges of the trapping regions, which are trapped at 850 km but not at 700 km.

In Fig. 7, the top panel shows the three-day total numbers of low laser energy shots in all locations, in the inner belt (SAA), in the northern and southern hemisphere footprints of the outer belt, and in all other regions (dominated by untrapped or quasi-trapped particles, usually GCRs). The bottom panel shows three-day averages of P6 observations in the same regions (P9 fluxes in the untrapped regions, to cleanly illustrate the GCR time variations). The P6 count rates are converted to >16 MeV proton fluxes in the inner belt and to >3 MeV electron fluxes in the outer belt using geometrical factors 2.3 and 0.13 cm^2 sr, respectively, derived from [12] using bowtie analysis [22]. Following a similar method, the P9 count rates are converted to >140 MeV proton GCR fluxes using a geometrical factor of 1.4 cm^2 sr. By converting count rates to fluxes in this figure, we illustrate how large the outer belt electron fluxes are compared to the inner belt proton fluxes. The large flux spikes in September 2017 and October 2021 are from spectrally hard solar energetic particle (SEP) events that caused ground-level increases in neutron monitors [23]. They were observed in all regions except the inner belt. Like GCRs, SEPs are untrapped or quasi-trapped yet penetrate readily into the outer belt, where electrons are trapped. CALIOP was placed in safe mode at the onset of the July and September 2017 and October 2021 SEP events, resulting in gaps in energy drop data during these events. For this reason, no evaluation of the effect of SEP fluxes on the laser is possible.

Apart from the onset of the phenomenon, the first large temporal fluctuation in low-energy shots was a relatively gradual increase by about a factor of 3, observed only in the SAA, that started around July 2017 and subsided by September 2018 (see Fig. 7). The second fluctuation, observed in all regions, was a larger increase that started in July 2019 and peaked before a sharp drop in the rate of low-energy shots in March 2020 (see Fig. 7). The sharp drop was relatively larger in the regions of lower-LET particles (outer belt electrons and GCRs) than in the higher-LET inner belt. This sharp drop was followed by a more gradual rise in the rate of low-energy shots that has stabilized since late 2020. The number of low-energy shots in the SAA flattened out in late 2020 while both the total low-energy shots (black curve) and the number of low-energy shots in the untrapped regions (red) continued to increase. This behavior suggests that the sensitivity to GCR fluxes continued to increase as the pressure decreased. It cannot be explained entirely by the increase in GCR fluxes, which as measured by the spatial average of the

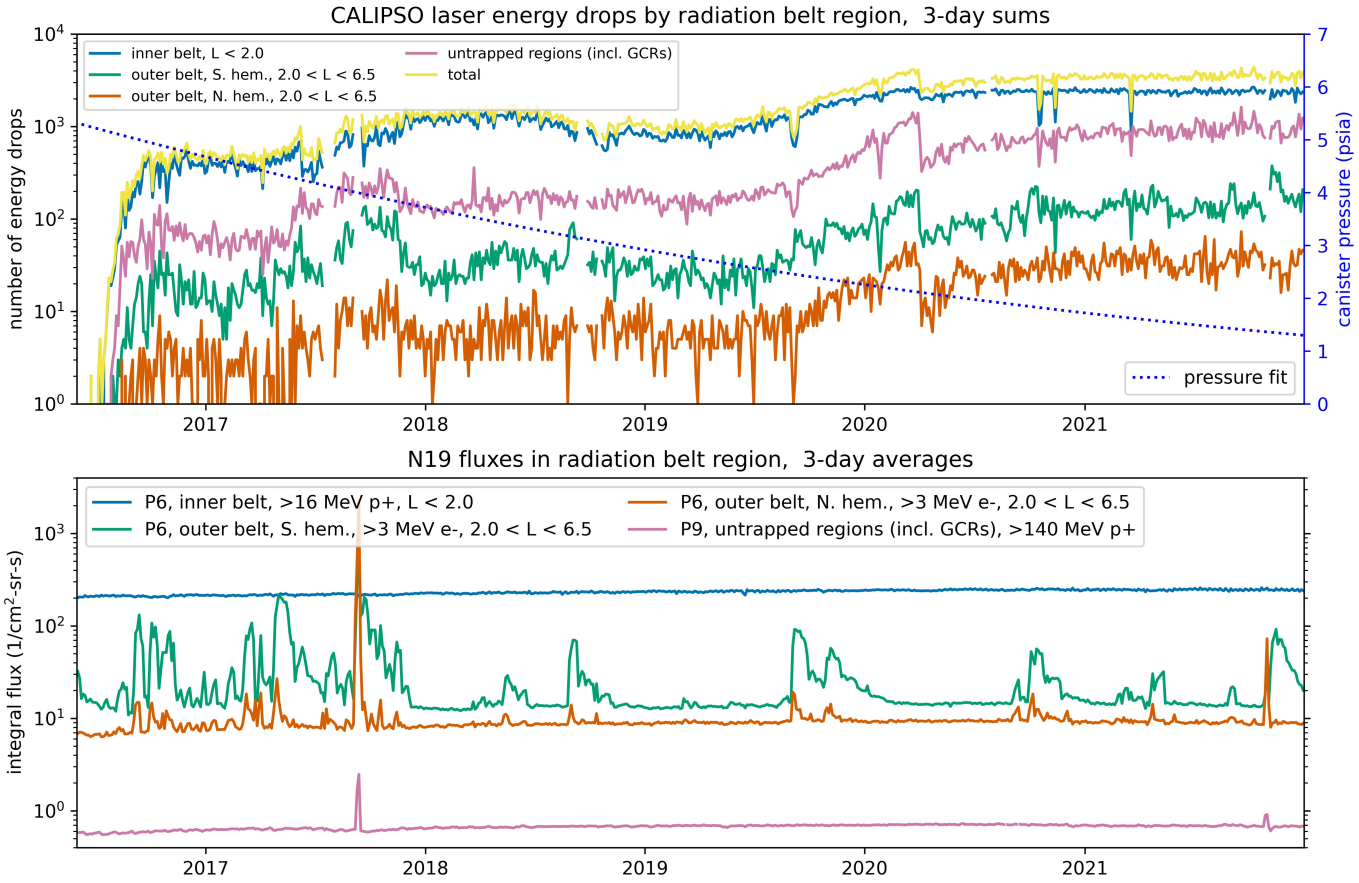

Fig. 7. CALIPSO low laser energy shot three-day numbers (top) and NOAA-19 integral flux three-day averages (bottom), June 2016–December 2021, spatially averaged over the indicated regions. The exponential fit to the canister pressure is represented as a dotted line superposed on the top and referred to the right-hand axis.

N19 P9 channel fluxes steadily increased by 25% over this period.

Two traces in the bottom panel represent the average fluxes in the southern and northern hemisphere footprints of the outer belt. The southern belt exhibits order-of-magnitude increases lasting several days to a month or more, due to radiation belt electron flux enhancements, with a relatively flat baseline from GCR fluxes (dominated by protons). (Because the electron geometrical factors were used to convert the P6 outer belt count rates to fluxes, the solar and GCR proton fluxes in the outer belt are too large by a factor of 10.) The northern hemisphere outer belt trace exhibits similar behavior at lower levels; the fluxes are lower because more of the trapped population has mirrored above the satellite due to the stronger magnetic field. Some of these correspond to short-term increases in the number of low-energy laser shots in the outer belt, as seen in Figs. 3 and 4. However, the dominant source of energy drops, the spatial average of the inner belt proton fluxes, increases only 20% from June 2016 to December 2021. There is no variation anywhere in the radiation fluxes that resembles either the large long-term energy-drop fluctuations or the sharp decrease in the number of energy drops identified above. Although, based on shielding considerations, we do not expect effects from <40 MeV protons and <3 MeV electrons, we ruled out the possibility of anomalous effects from lower-energy particles by analyzing the time series of lower-energy fluxes from the N19 MEPED telescopes, covering electron energies from >30 to >612 keV and proton energies from 30 to 6900 keV and >6900 keV.

V. Discussion

The comparisons shown above reveal that the CALIPSO low laser energy shots are associated spatially with three energetic charged particle populations: 1) 10's of MeV protons in the inner belt (SAA); 2) background levels of GCRs whose intensity increases from the equator toward the poles; and 3) MeV electrons in the outer belt, which vary on much shorter time scales than the other two sources. These spatial associations are clear. The observed association with MeV electrons provides further support to the conclusion that the low laser energy shots are not caused by SEE in the laser electronics. The spatial comparisons in the SAA also reveal that the size of the low-energy shots is related in part to the flux levels. Larger energy drops are observed in the center of the SAA, where the proton fluxes are greater (Figs. 3 and 4). This finding suggests that as ionization accumulates in the canister gas from multiple proton hits, the likelihood of a large laser energy drop increases. Also, it suggests that the ionization recombination time constant at the observed pressures is

comparable to or longer than the arrival rate of the ionizing radiation, causing the percent ionization of the canister gas to track the local flux levels.

Despite the clear spatial associations with distinct charged particle populations in low-Earth orbit (LEO) (the inner and outer belts and GCRs), the largest temporal fluctuations in the rate of low laser energy shots cannot be explained by changes in the charged particle populations. These fluctuations included: 1) a relatively gradual yet large (∼3x) increase that started around July 2017 and subsided by September 2018 and 2) a much larger increase that started in June 2019, was interrupted by a sharp drop in March 2020, continued thereafter more gradually, and has stabilized since late 2020 (see Fig. 7). No changes in the radiation populations were observed to be associated with these increases in the rate of low-energy shots. Therefore, an additional mechanism internal to the canister is likely. After years of outgassing, it is likely that the canister gas is no longer purely the original dry air mixture. When identifying candidates for internal mechanisms, one candidate is the possibility that organic molecules in the outgassing products are polymerized onto the laser by ionizing radiation, and that changes in the depth and distribution of the deposits over time could be causing some of the time-varying behavior. In an example involving another kind of instrument, proportional counters filled with methane-noble gas mixtures (5%–10% methane) exhibit changes in gain due to polymerization of the methane onto the anode wire through exposure to ionizing radiation [24]. However, since the high laser pulse energy is likely to damage contaminated surfaces, and no permanent (catastrophic) decrease is observed in the output energy, the detailed mechanism remains to be discerned.

These large fluctuations are superposed on the longer-term increase in the number of low-energy shots, which commenced in June 2016. This sudden start is not associated with any change in the radiation environment. The only short-term, large changes in the radiation environment at N19 altitude occurred in the outer belt due to increases in MeV electron fluxes, and these contributed only in a minor way to the global rates of low-energy shots. The continuous, approximately exponential decrease in the redundant canister pressure (by a factor of 3.6 from launch to June 2016, and a factor of 4.6 from June 2016 to December 2021) is the only known long-term change that can be associated with the appearance of this phenomenon. The range of canister pressures between June 23, 2016, and December 31, 2021, was similar to the atmospheric pressure range between 8 and 18 km altitudes, in the upper troposphere and lower stratosphere. The phenomenon observed here may be related to the physics of upper atmospheric discharges, although the physical scales are different. The degree of ionization in the canister gas and the recombination chemistry of this partially-ionized gas at low pressures are also important aspects of the problem that should be investigated in the future.

VI. Conclusion

The CALIPSO CALIOP lidar low-energy shot phenomenon first appeared when the canister air pressure decreased to 35 kPa. By the end of December 2021, the canister pressure was 7.6 kPa. The low-energy shots are spatially associated with the extensions of both the inner and outer radiation belts into LEO and with GCRs, suggesting that the radiation is penetrating the canister shielding and partially ionizing the gas. (Since the lidar is placed into safe mode during SEP events, the effect of SEPs cannot be determined.) While the majority of the low-energy shots take place in the inner belt (SAA), there are clear spatial associations with enhanced outer belt electron fluxes and with GCRs. Within the SAA, larger proton fluxes toward the center of the SAA are associated with larger laser energy drops. As canister pressure has decreased, GCRs and radiation belt electrons have become more effective in causing larger laser energy drops. Time variations in outer belt electron fluxes are associated with small, short-term variations in the number of low-energy shots. However, some longer-term, large time variations cannot be explained by changes in charged particle fluxes or the monotonic decrease in canister pressure. This observation indicates that an unidentified mechanism internal to the canister also affects the interaction of the laser with the penetrating radiation in the gas.

Acknowledgment

The NOAA-19 SEM-2 data are available from the NOAA National Centers for Environmental Information (https://www.ngdc.noaa.gov/stp/satellite/poes/dataaccess.html). The CALIPSO data are available from the NASA Langley Research Center (https://www-calipso.larc.nasa.gov/products/). Documentation on the SpacePy, "alphashape," and "shapely" Python libraries can be found at https://spacepy.github.io/, https://alphashape.readthedocs.io, and https://shapely.readthedocs.io, respectively. The authors would like to thank R. Arentz for bringing [24] to our attention and R. Redmon for reviewing an earlier version of the manuscript.

References

[1] K. A. Label *et al.*, "Proton-induced transients in optocouplers: In-flight anomalies, ground irradiation test, mitigation and implications," *IEEE Trans. Nucl. Sci.*, vol. 44, no. 6, pp. 1885–1892, Dec. 1997, doi: 10.1109/23.658957.

[2] D. Falguere *et al.*, "In-flight observations of the radiation environment and its effects on devices in the SAC-C polar orbit," *IEEE Trans. Nucl. Sci.*, vol. 49, no. 6, pp. 2782–2787, Dec. 2002, doi: 10.1109/TNS.2002.805380.

[3] G. Jaross *et al.*, "OMPS limb profiler instrument performance assessment," *J. Geophys. Res., Atmos.*, vol. 119, no. 7, pp. 4399–4412, Apr. 2014, doi: 10.1002/2013JD020482.

[4] C. Cao *et al.*, "Overview of Suomi NPP VIIRS performance in the last 2.5 years," *Proc. SPIE*, vol. 9264, Nov. 2014, Art. no. 926402, doi: 10.1117/12.2068991.

[5] T. P. Lee *et al.*, "Abnormal signatures recorded by FORMOSAT-2 and FORMOSAT-3 over south Atlantic Anomaly and polar region," *Terr. Atmos. Ocean. Sci.*, vol. 25, no. 4, pp. 573–580, Aug. 2014, doi: 10.3319/TAO.2014.02.26.01(AA).

[6] R. K. Schaefer *et al.*, "Observation and modeling of the south Atlantic Anomaly in low Earth orbit using photometric instrument data," *Space Weather*, vol. 14, no. 5, pp. 330–342, May 2016, doi: 10.1002/2016SW001371.

[7] W. H. Hunt, D. M. Winker, M. A. Vaughan, K. A. Powell, P. L. Lucker, and C. Weimer, "CALIPSO Lidar description and performance assessment," *J. Atmos. Ocean. Technol.*, vol. 26, no. 7, pp. 1214–1228, Jul. 2009, doi: 10.1175/2009JTECHA1223.1.

[8] NASA Langley Research Center. (Oct. 10, 2018). *CALIPSO Low Laser Energy Technical Advisory for Data Users*. [Online]. Available: https://www-calipso.larc.nasa.gov/resources/calipso users guide/advisory/advisory2018-10-10-CALIPSOLaser EnergyTechnical-Advisory Ver03.pdf

[9] M. Vaughan *et al.*, "CALIPSO data management system data products catalog," Release 4.92, NASA Langley Res. Center, Hampton, VA, USA, Tech. Rep. PC-SCI-503, 2020. [Online]. Available: https://www-calipso.larc.nasa.gov/products/CALIPSO DPC Rev4x93.pdf

[10] D. S. Evans and M. S. Greer, "Polar Orbiting Environmental Satellite Space Environment Monitor-2: Instrument descriptions and archive data documentation," NOAA Space Environ. Center, Boulder, CO, USA, NOAA Technical Memorandum OAR SEC-93, Dec. 2000. [Online]. Available: https://satdat.ngdc.noaa.gov/sem/poes/docs/sem2_docs/2006/SEM2v2.0.pdf

[11] J. Green, "External users manual POES/MetOp SEM-2 processing," Version 1.0, NOAA Nat. Geophys. Data Center, Boulder, CO, USA, Tech. Rep., Mar. 2013. [Online]. Available: https://ngdc.noaa.gov/stp/satellite/poes/docs/NGDC/ExternalUsersManualPOESMetOpSEM-2processingV1.pdf

[12] T. E. Cayton, "Numerical modeling of the omnidirectional spectrometer of the medium energy proton and electron detector (MEPED) subsystem of the space environment monitor (SEM) that flew aboard several polar orbiting satellites," Los Alamos Nat. Lab., Los Alamos, NM, USA, Tech. Rep. LA-UR-07-7314, Nov. 2007.

[13] D. Evans, H. Garrett, I. Jun, R. Evans, and J. Chow, "Long-term observations of the trapped high-energy proton population (L < 4) by the NOAA polar orbiting environmental satellites (POES)," *Adv. Space Res.*, vol. 41, no. 8, pp. 1261–1268, Jan. 2008, doi: 10.1016/J.ASR.2007.11.028.

[14] D. Boscher, A. Sicard-Piet, D. Lazaro, T. Cayton, and G. Rolland, "A new proton model for low altitude high energy specification," *IEEE Trans. Nucl. Sci.*, vol. 61, no. 6, pp. 3401–3407, Dec. 2014, doi: 10.1109/TNS.2014.2365214.

[15] D. Boscher, S. Bourdarie, V. Maget, A. Sicard-Piet, G. Rolland, and D. Standarovski, "High-energy electrons in the inner zone," *IEEE Trans. Nucl. Sci.*, vol. 65, no. 8, pp. 1546–1552, Aug. 2018, doi: 10.1109/TNS.2018.2824543.

[16] C. McIlwain, "Magnetic coordinates," *Space Sci. Rev.*, vol. 5, pp. 585–598, Aug. 1966, doi: 10.1007/BF00167327.

[17] D. N. Baker *et al.*, "Multiyear measurements of radiation belt electrons: Acceleration, transport, and loss," *J. Geophys. Res., Space Phys.*, vol. 124, no. 4, pp. 2588–2602, Apr. 2019, doi: 10.1029/2018JA026259.

[18] D. Boscher, S. Bourdarie, P. O'Brien, and T. Guild. (2004–2008). *IRBEM Library V4.3*. [Online]. Available: https://sourceforge.net/projects/irbem/

[19] S. K. Morley, J. Koller, D. T. Welling, B. A. Larsen, M. G. Henderson, and J. T. Niehof, "SpacePy—A Python-based library of tools for the space sciences," in *Proc. 9th Python Sci. Conf.*, Austin, TX, USA, 2011, pp. 67–72. [Online]. Available: https://conference.scipy.org/proceedings/scipy2010/

[20] G. P. Ginet, B. K. Dichter, D. H. Brautigam, and D. Madden, "Proton flux anisotropy in low Earth orbit," *IEEE Trans. Nucl. Sci.*, vol. 54, no. 6, pp. 1975–1980, Dec. 2007, doi: 10.1109/TNS.2007.910041.

[21] J. G. Roederer, *Dynamics of Geomagnetically Trapped Radiation*, Berlin, Germany: Springer-Verlag, 1970, p. 107.

[22] R. W. Fillius and C. E. McIlwain, "Measurements of the Jovian radiation belts," *J. Geophys. Res.*, vol. 79, no. 25, pp. 3589–3599, Sep. 1974, doi: 10.1029/JA079i025p03589.

[23] P. Jiggens *et al.*, "*In situ* data and effect correlation during September 2017 solar particle event," *Space Weather*, vol. 17, pp. 99–117, Nov. 2019, doi: 10.1029/2018SW001936.

[24] A. Smith and M. J. L. Turner, "Lifetime of proportional counters filled with xenon-methane and argon-methane," *Nucl. Instrum. Methods Phys. Res.*, vol. 192, nos. 2–3, pp. 475–481, Feb. 1982, doi: 10.1016/0029-554X(82)90862-X.